Electronic Supplementary Material (ESI) for Energy & Environmental Science.
This journal is © The Royal Society of Chemistry 2021

Supplementary information

Monitoring battery electrolyte chemistry via in-operando tilted fiber Bragg grating sensors

Jiaqiang Huang,[ab] Xile Han,[c] Fu Liu,[d] Charlotte Gervillié,[ab] Laura Albero Blanquer,[abe] Tuan Guo*[c] and Jean-Marie Tarascon*[abe]

[a] Chimie du Solide et de l'Energie, UMR 8260 CNRS, Collège de France, 75005 Paris, France.

[b] Réseau sur le Stockage Electrochimique de l'Energie (RS2E), FR CNRS 3459, 80039 Amiens, France.

[c] Institute of Photonics Technology, Jinan University, Guangzhou 510632, China.

[d] Department of Electronics, Carleton University, Ottawa, K1S 5B6, Canada.

[e] Sorbonne Université, UPMC Paris 06, 75005 Paris, France.

*Emails: tuanguo@jnu.edu.cn (T. G.); jean-marie.tarascon@college-de-france.fr (J.-M. T.)

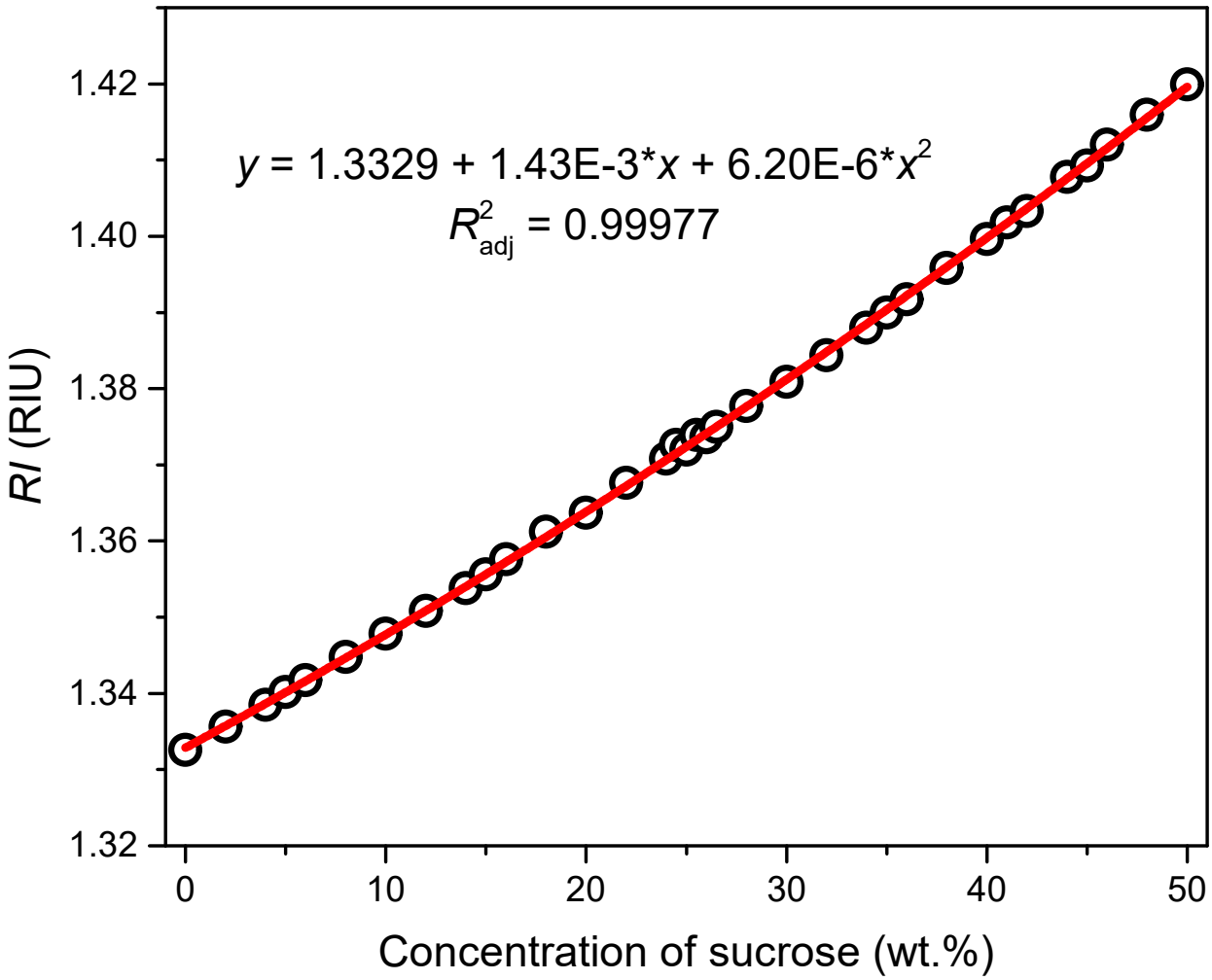

Fig. S1 Refractive index of sucrose solutions at different concentrations (0-50 wt.%). The Refractive indices were measured by a commercial refractometer (Reichert Technologies, AR200, resolution: ±0.0001 RIU) at recorded temperatures of ~23.0 °C. The *RI* increases with the sucrose concentration (black circles), which is quadratically regressed (red line) with a R_{adj}^2 = 0.99977.

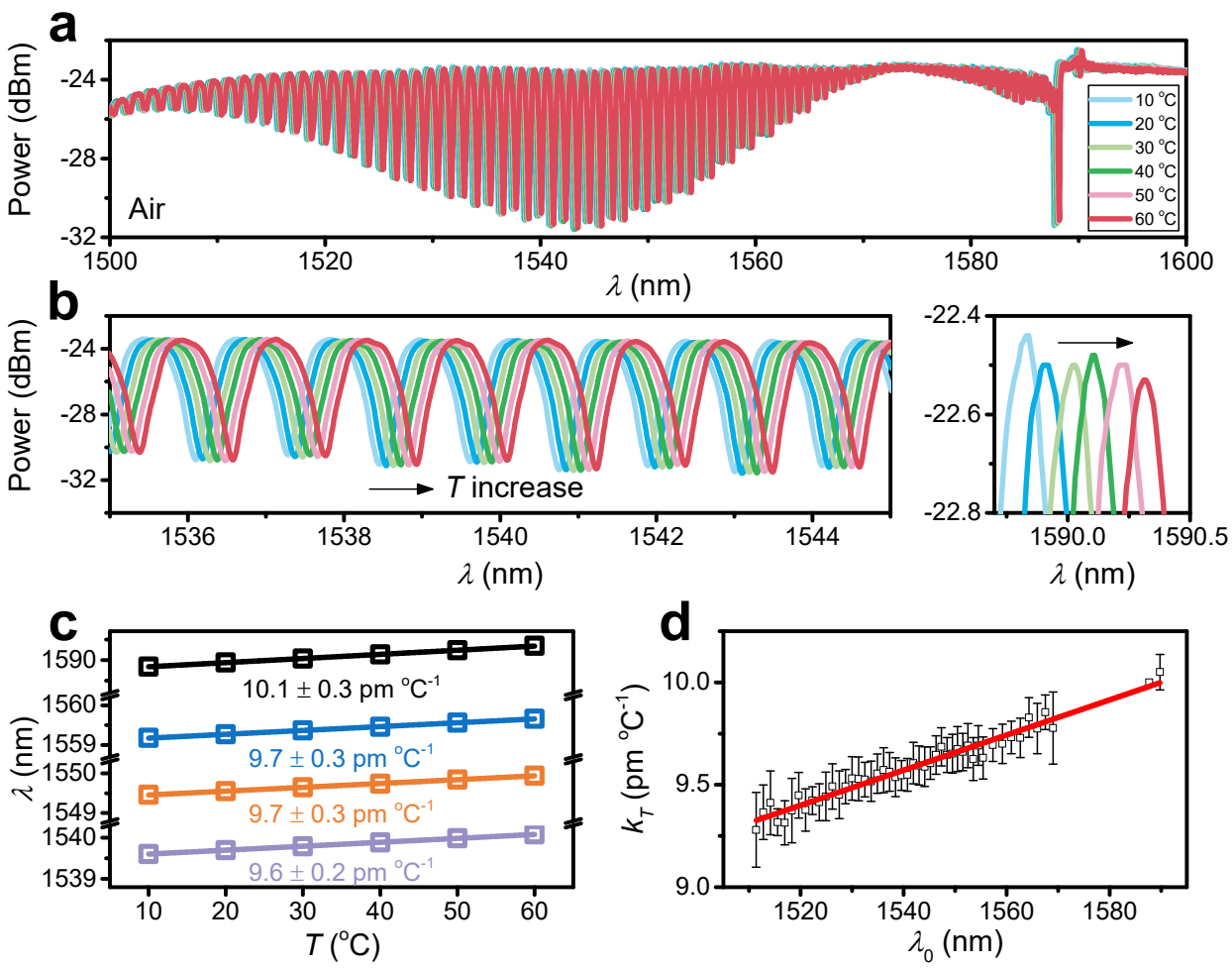

Fig. S2. Response spectra of TFBG to temperature. (a) The full spectra of TFBG at 10 to 60 °C in 10 °C increments in the air (refractive index: ~1.000). (b) Enlarged spectra of the claddings at ~1,540 nm (left panel) and Bragg (right panel) resonances. The arrows indicate the direction of wavelength change upon the increase of temperature. While the wavelengths red shift with T, the amplitudes do not change significantly. (c) The wavelengths of the claddings at ~1,560 (blue), ~1,550 (orange), and ~1,540 (purple) nm and Bragg resonances (~1,590 nm, black) in response to temperature. The raw data (scatters) are linearly fitted (lines) with the slopes, that is, the thermal sensitivity (k_T). The uncertainty of the slope is given by three standard deviations (±3σ). (d) The correlation between k_T and the pristine resonance wavelength (λ_0 taken at 10 °C). The error bars were obtained by the linear regression at each resonance, see some examples in (c). A linear regression was performed (red line), showing a R_{adj}^2 = 0.9582. Interestingly, the k_T linearly increases with the resonance wavelength, due to the differences in the thermo-optic coefficients ($\partial n/\partial T$) and effective refractive index between the cladding and the Bragg resonances, see the detailed analysis in the literature[S1]. The varied k_T with wavelengths leads to the shift of wavelength separation shown in Fig. 2d.

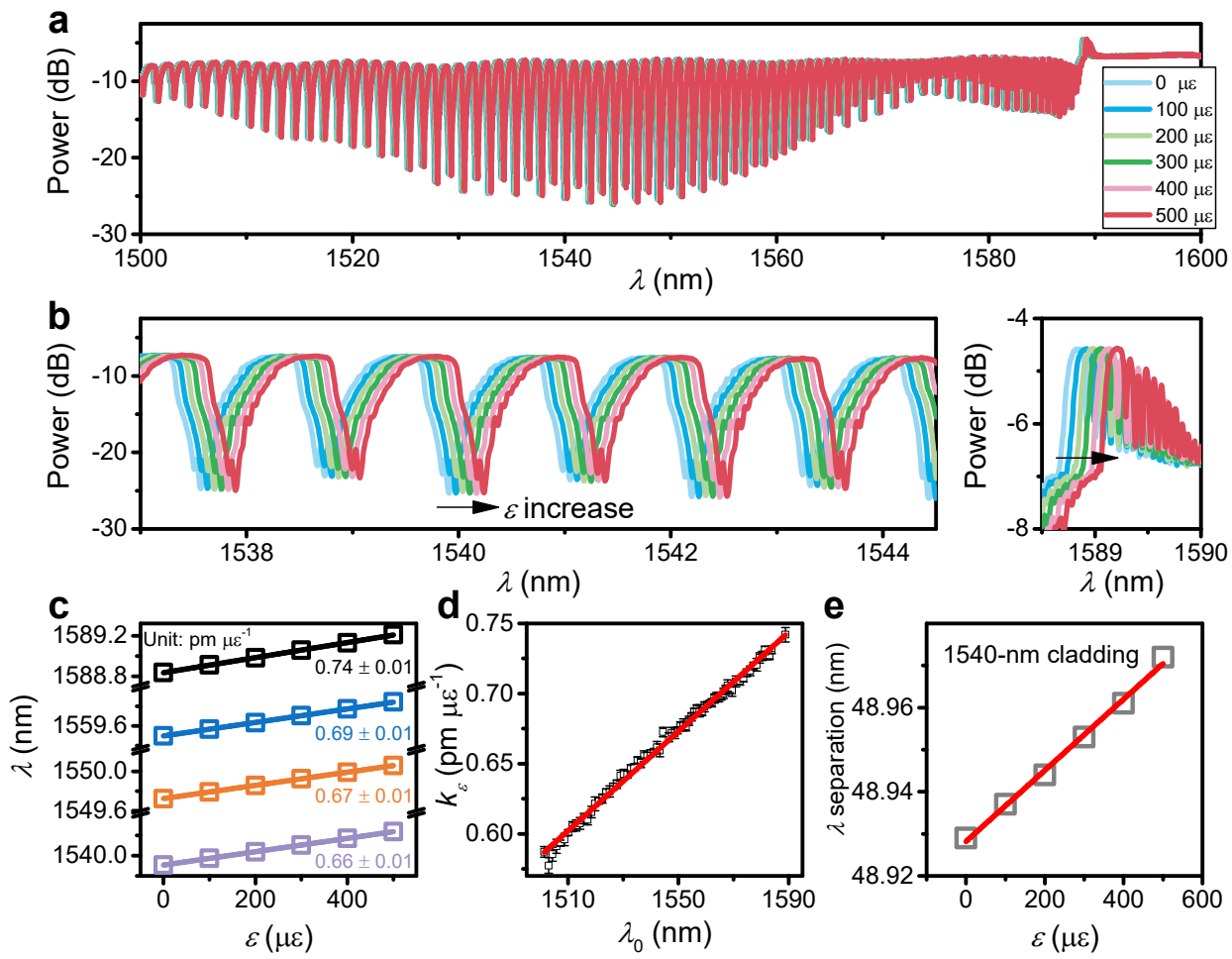

Fig. S3 Response spectra of TFBG to strain. (a) The full spectra of TFBG upon the strain from 0 to 500 με in 100 με increments in air. (b) Enlarged spectra of the claddings at ~1,540 nm (left panel) and Bragg (right panel) resonances. The arrows indicate the direction of wavelength change upon the increase of strain. While the wavelength red shifts with ε, the amplitudes do not change. (c) The wavelengths of the claddings at ~1,540 (purple), ~1,550 (orange), ~1,560 nm (blue), and Bragg resonances (~1,589 nm, black) in response to ε as shown in (a and b). The texts are the rate constant response to ε (k_ε) with a unit of pm $\mu\varepsilon^{-1}$ for each resonance, and the uncertainty is three standard deviations ($\pm 3\sigma$). k_ε increases with the wavelengths of resonances, owing to the larger wavelength and smaller photoelastic coefficients of the resonances at larger wavelengths[S2]. The k_ε of the Bragg resonance (0.74 pm $\mu\varepsilon^{-1}$) is close to the one of FBG written in SMF (SMF-FBG) we measured previously[S3] (0.84 pm $\mu\varepsilon^{-1}$), while the difference may stem from the variation of fibers and the measurement uncertainty. (d) The correlation between k_ε and the pristine resonance wavelength (λ_0 taken in the strain-free state). The error bars were obtained by the linear regression at each resonance, see some examples in (c). A linear regression was performed (red line), showing a R_{adj}^2 = 0.9935, which may be explained by the governing equation[S2] controlled by wavelengths and photoelastic coefficients. The varied k_ε among different resonances offer the opportunities to decoupling T, ε, and RI simultaneously, for example, by taking the wavelength shifts of three resonances to solve these three unknowns. (e) The wavelength separation between the Bragg and

the cladding resonances at ~1,540 nm as a function of ε. The red line is a linear regression with a R_{adj}^2 = 0.9944, and this trend is consistent with the literature[S2].

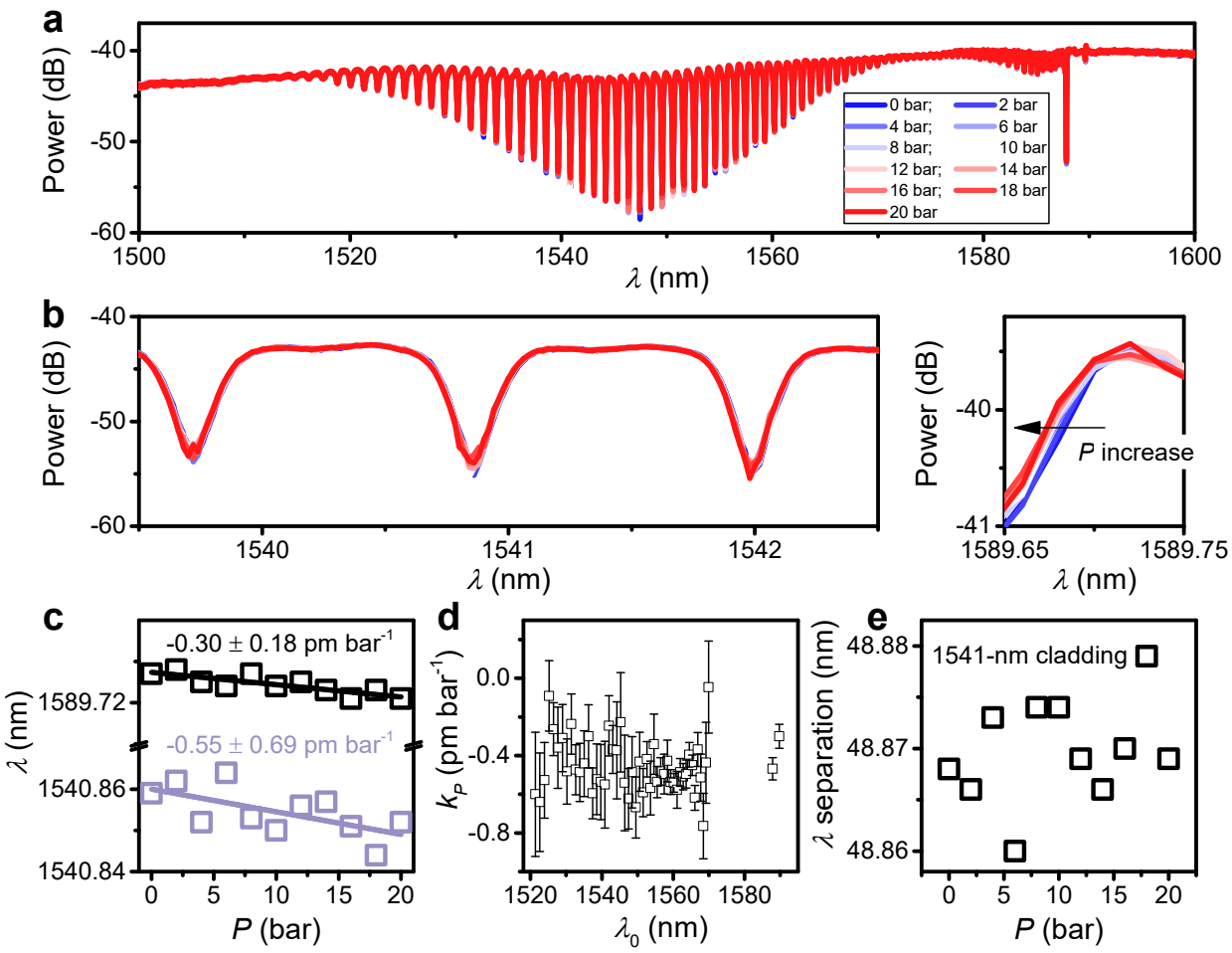

Fig. S4 Response of TFBG to pressure. (a) The full spectra of TFBG upon the pressure from 0 to 20 bar in 2 bar increments in water. 20 bar was selected here, because it is approximately the pressure limit of safety device for 18650 cells. (b) Enlarged spectra of the claddings at ~1,540 nm (left panel) and Bragg (right panel) resonances. The arrow indicates the direction of wavelength change upon the increase of pressure. The changes are insignificant (left panel) in comparison to the ones of T and ε in Fig. S2 and Fig. S3, though we can still see some blue shifts of the Bragg resonance upon the pressure increase (right panel, arrow). Note that the RI of water increases with P by a coefficient of ~10^{-5} RIU bar^{-1} as reported[S4]. We expected a few pm errors in wavelength for those cladding with similar $n_{eff,clad}(i)$ to water, because only these claddings are highly sensitive to RI change in this range as seen in Fig. 2c. (c) The wavelengths of the cladding at ~1,540 nm (purple) and Bragg resonances (~1,590 nm, black) in response to P shown in (a and b). The texts are the rate constant response to P (k_P) for each resonance, and the uncertainty is three times standard deviation (±3σ). The data is relatively noise for the cladding mode; nevertheless, the trends are clear that the wavelength decreases with P. The k_P of the Bragg resonance (-0.30 pm bar^{-1}) is similar to what we previously measured for SMF-FBG (-0.34 pm bar^{-1})[S3]. (d) The k_P of the resonances at different wavelengths with error bars. Though noise, the k_P is roughly -0.4 pm bar^{-1} for the resonances, and the wavelength dependence is not clear. Theoretically, we expected an opposite trend to strain in Fig.

S3d because the hydraulic pressure induced deformation of fiber and applied a negative tensile strain[S5]. The invisibility of the trend may come from the noise of the data and further the minor deformation of SMF to hydraulic pressure[S5]. (e) The wavelength separation between the Bragg and the cladding resonances at ~1,540 nm as a function of *P*. No clear trend is seen, which is ascribed to the minor deformation of SMF in response to hydraulic pressure. This suggests that the pressure effect on TFBG written in SMF is negligible in 18650 cells. Thus, in light of our previous work[S3], we are exploring to write TFBG on microstructured optical fibers[S6].

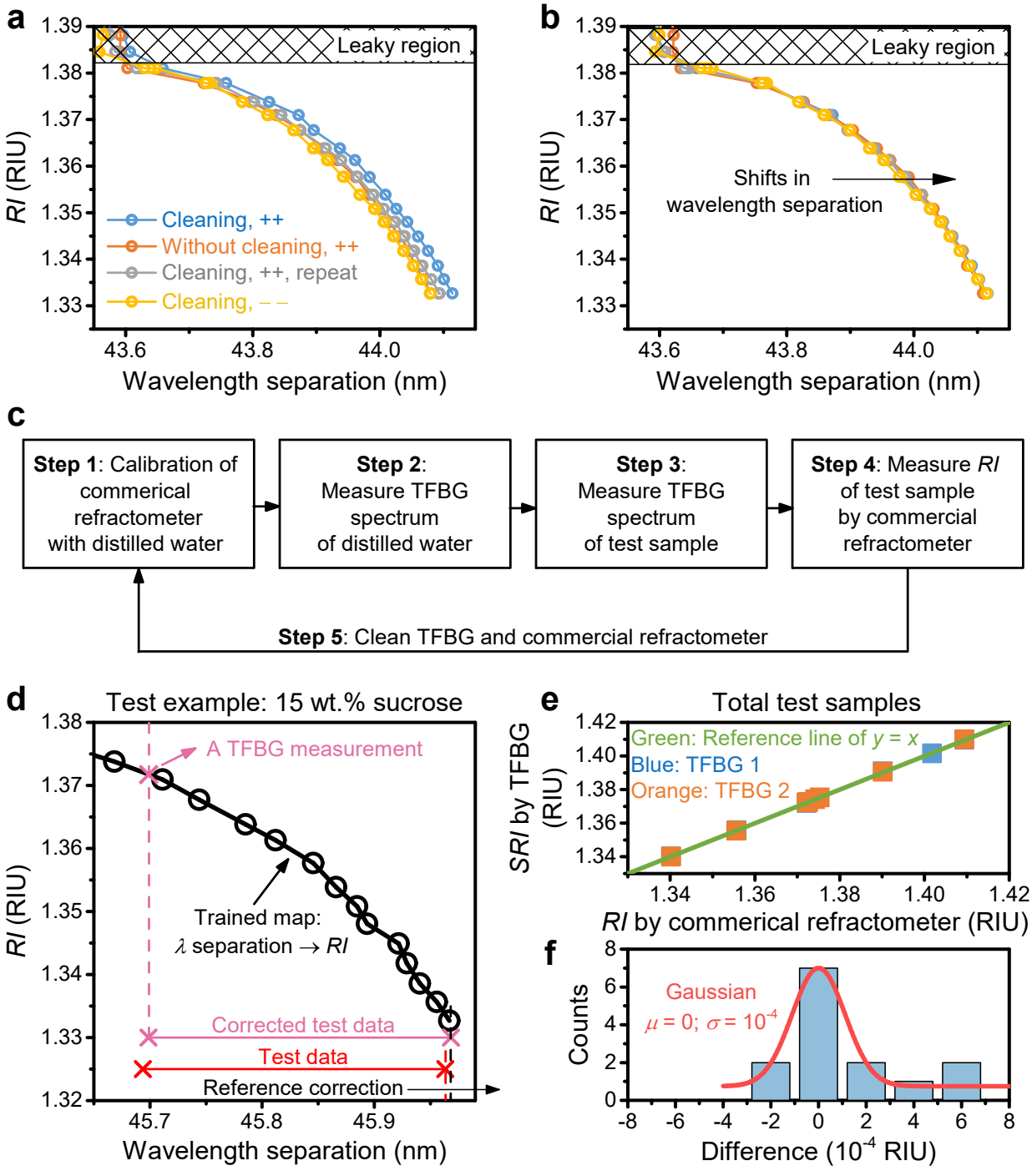

Fig. S5 Correction of TFBG against a reference. (a) The calibration curves of the wavelength separation of identical cladding resonance with respect to *RI* in different calibration experiments of the same TFBG. The leaky region is marked by meshes, where the wavelength separation does not vary with *RI*. Four experiments were conducted, including (1) With water cleaning, increasing the concentration of sucrose from 0 to 50 wt.%, blue curve; (2) Without water cleaning, increasing the concentration of sucrose, orange curve; (3) Same conditions as (1), repeat experiment, grey curve; (4) With water cleaning, decreasing the concentration of sucrose from 50 to 0 wt.%, yellow curve. These four curves do not overlap with each other, indicating the possible drift of the TFBG sensor. (b) Curves in (a) that were shifted in the wavelength separation. The shifted four curves are superimposed with each other, meaning that drift may be corrected by the wavelength separation. This poses the necessity to correct the wavelength separation of the TFBG sensor by a standard solution (*e.g.*, distilled water) prior to each measurement as done in the commercial refractometer. (c) The flow chart to test the correction method of wavelength separation for TFBG. A batch of new samples (test samples), which were not measured in (a, training samples), were prepared to test the methodology. (d) An example of correction of wavelength separation with the 15 wt.% sucrose solution. We plotted one trained map (wavelength (λ) separation → *RI*, black scatters with interpolated lines) from (a). We obtained wavelength separation data (red scatters) of the reference (distilled water, "Step 2" in c) and the test sample ("Step 3" in c). The just measured wavelength separation of the reference is not equal to the one in the trained map, implying the drift of TFBG. To correct this drift, the just measured two wavelength separations were shifted (black arrow). This produces a corrected wavelength separation of the test sample (purple cross). By applying the corrected wavelength separation into the trained map, we calculated the *RI* of the test sample from TFBG. (e) The comparison of *RI* of the test samples measured by TFBG and commercial refractometer. Two TFBGs (blue and orange scatters) were tested using the correction method. The green line indicates a reference where both TFBG and commercial refractometer give the same results. The more the scatters deviate from the green line, the more difference between the results of TFBG and commercial refractometer. (f) The distribution histogram of the measured differences in *RI* by TFBG and commercial refractometer based on 16 tests. The distribution is fitted by a Gaussian function (red line), giving a mean (μ) of 0 and a standard deviation (σ) of 10^{-4} RIU. This result supports the accuracy of TFBG measurements with the correction method. In the battery measurements, we cannot use distilled water but the electrolyte as the reference for the wavelength separation correction.

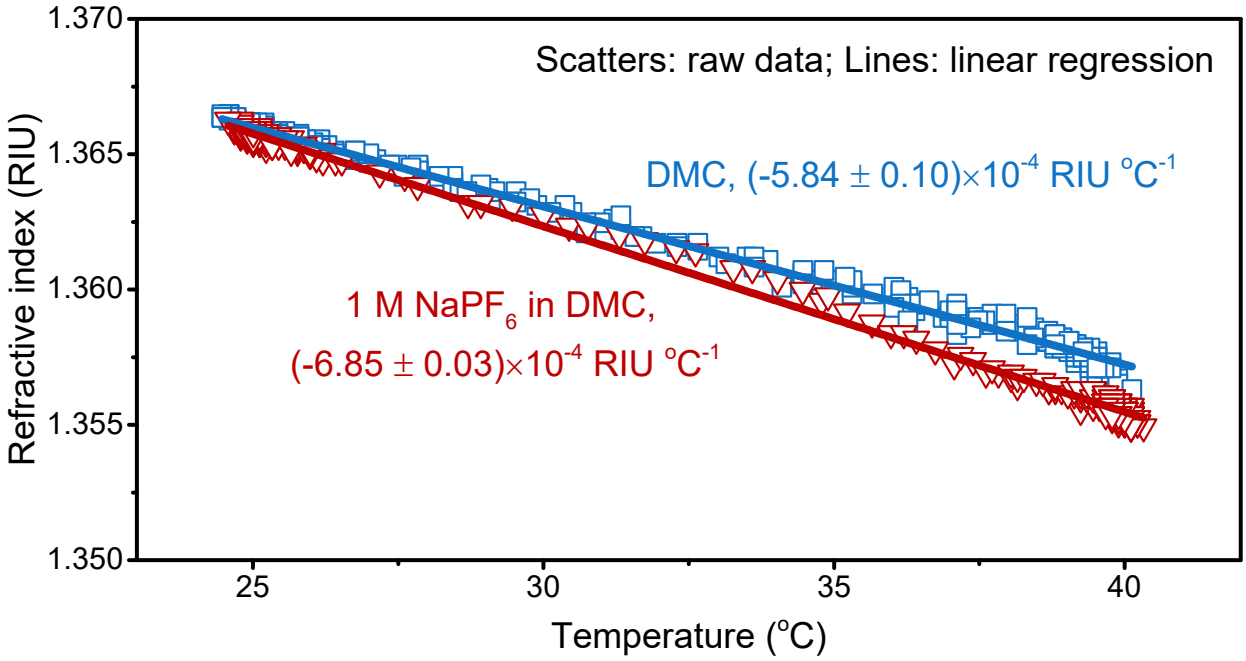

Fig. S6 Temperature coefficient of *RI* of electrolytes. The *RI* of DMC (blue) and 1 M $NaPF_6$ in DMC (red) measured by TFBG as a function of temperature. The raw data and the linear regression are represented by scatters and lines, respectively. The slopes of the lines, *i.e.*, the temperature coefficients of *RI* (d*RI*/d*T*), are shown in text with uncertainties (±3σ).

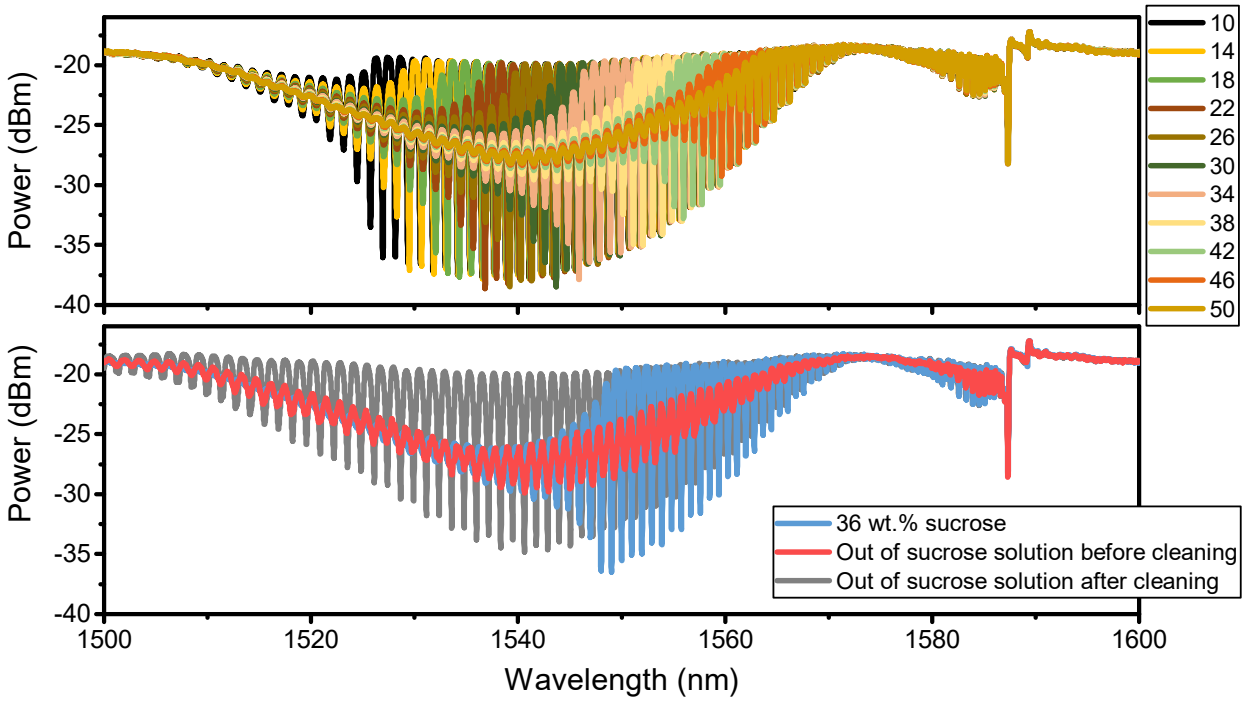

Fig. S7 TFBG spectra with particles on the cladding surface. The top panel shows the spectra of TFBG immersed in sucrose solutions with concentrations ranging from 10 to 50 wt.% (see the legend). The resonance amplitudes are suppressed gradually from short to long wavelengths. The bottom panel gives

the spectra of TFBG: (1) Immersed in a 36 wt.% sucrose solution, blue line; (2) Just taken out of the 36 wt.% sucrose solution in air, red line; (3) In air after the distilled water cleaning to remove the sucrose remains, grey line. The distinguishing feature of the red spectra from the others is the simultaneous amplitude suppression of most of the cladding resonances. Interestingly, after the cleaning by distilled water, the TFBG spectrum in the air (grey line) restored the amplitudes of resonances, indicating that some sucrose (and likely some water) remained on the cladding before cleaning. This reminds the previous study with similarly suppressed spectra, where the silver nanoparticles were deposited on TFBGs[S7]. The suppression may come from the scattering or absorption of photonic energy by the particles[S7]. Consequently, the red line may indicate the deposition of some particles on the TFBG's cladding, which scatter or absorb the photonic energy so that the resonance amplitudes were suppressed. Because Fig. 4b and c show similar characteristics to the red line, it probably suggests that the excessive decomposition of liquid DMC that may saturate the electrolytes with solid particles such as by-products and/or $NaPF_6$.

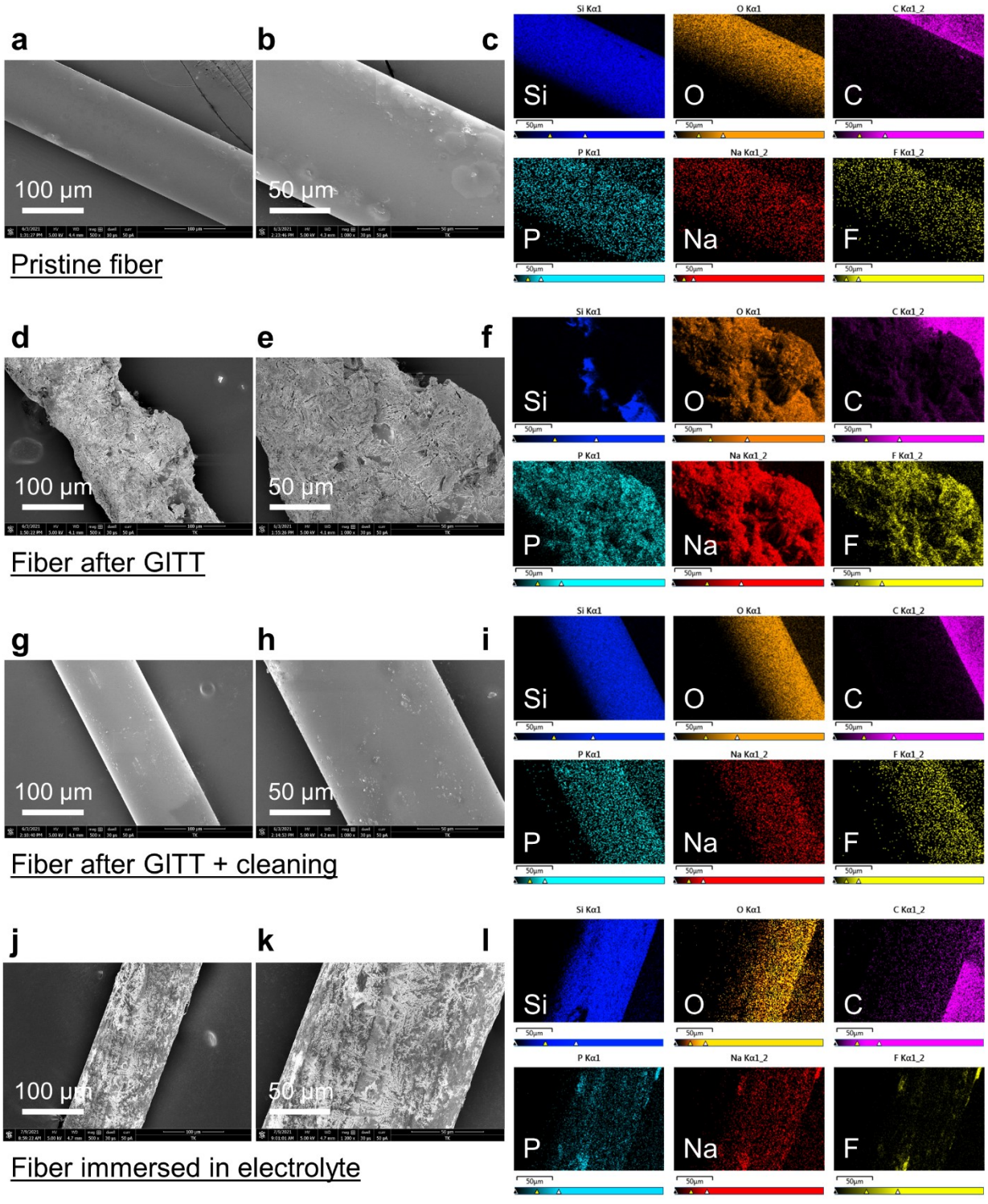

Fig. S8 The scanning electron microscope (SEM) images of fibers. (a-l) The SEM images of the pristine fiber (a and b), the fiber after the GITT test (d and e), the cleaned fiber with ethanol after GITT (g and h), and the fiber immersed in electrolyte for two weeks (j and k), together with the corresponding energy-dispersive X-ray spectroscopy (EDX) mappings in (c), (f), (i) and (l), respectively. Compared to the pristine fiber (a and b), the fiber after the GITT (d and e) shows rough surfaces, indicating the depositions of

particulates on the fiber's cladding. Besides, the EDX mapping of the fiber after the GITT (f) further manifests the disappearance of Si signals in most of the surface region, verifying the hypothesis that some materials were deposited on the fiber. Remarkably, the intensity textures of O, P, Na, and F elements in (f) agree with the morphology of the surface deposits in (e). This provides hints to the composition of the deposits, and $NaPF_6$ and its decomposition products are highly suspicious. Besides, there is only minor intensity of C element on fibers in (f), but it is more obvious than the ones in (c) and (i). Note that the C element outside fiber originated from the carbon tape. Thus, the DMC-derived products such as sodium methoxide and sodium methyl carbonate may be parts of the deposits; however, their richness is not supported by EDX. Considering the weakness of EDX in light elements such as C, unfortunately, we cannot conclude the composition of deposits on the fiber after GITT (d-f) solely by EDX. Lastly, we cleaned the fiber after GITT with ethanol (g-i), and the images (g and h) and EDX mapping (i) are similar to the pristine fiber (a-c) rather than the one without cleaning (d-f). This implies that the bonding of the deposits to the fiber surface is weak. Besides, we could not spot visible increases in the roughness of the fiber surface (g and h) in comparison to the pristine one (a and b); in other words, the corrosion of fiber by side products such as HF was not found. To clarify whether the deposits in (d-e) are associated with the electrolyte degradation, one fiber was immersed in the electrolyte for two weeks before being taken out for the SEM in (j-k). On the contrary, much less deposits are seen in (j and k) with abundant Si and poor P, Na, and F elements on the fiber surface (l), confirming the deposition of side products on the fiber surface after the GITT test (d-e).

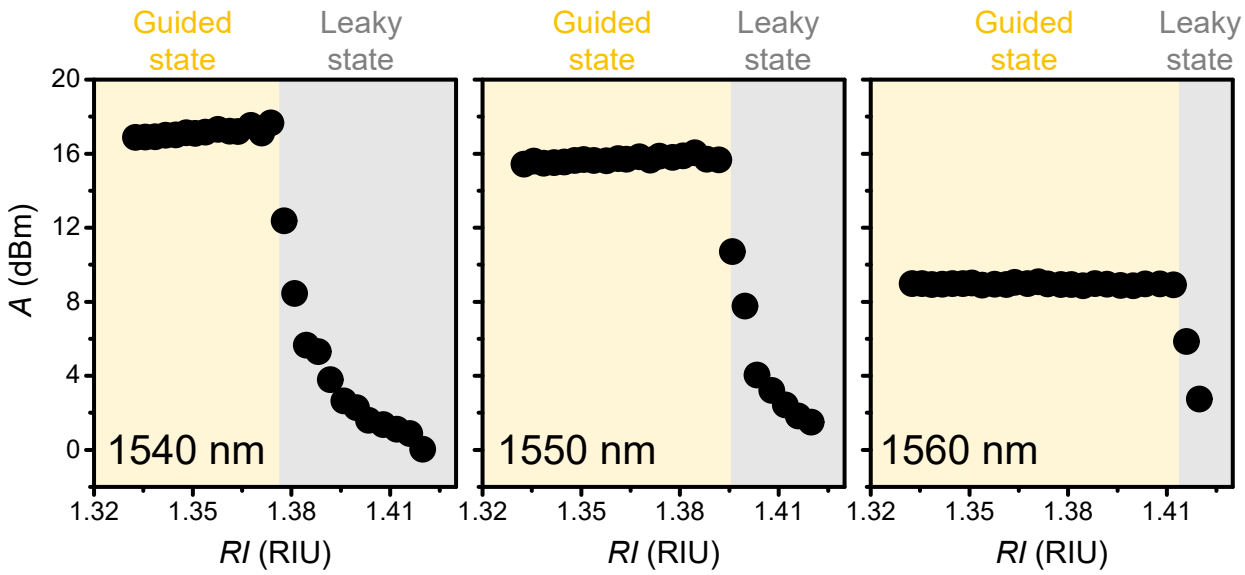

Fig. S9 The peak-to-peak amplitude (*A*) in response to *RI*. The *A* at three wavelength positions, including 1,540 (left), 1,550 (middle), and 1,560 (right) nm, were selected and shown here. These results were derived from the same data for Fig. S7, top. The yellow and grey backgrounds indicate the resonances are in the guided and the leaky states (see Fig. 4d), respectively. Interestingly, the resonance at a higher wavelength has a larger yellow region of the guided state, because the $n_{eff,clad}(i)$ increases with $\lambda_{clad}(i)$, see eqn (1). The *A* is nearly constant when the resonances are in the guided states.

Table S1. The *RI* of electrolyte-related samples measured by the commercial refractometer.

Sample	Measured *RI* (RIU), *T* (°C)*	Estimated *RI* at 25 °C (RIU)#
DMC	1.3675, 22.4	1.3660
DMC with saturated sodium methoxide	1.3674, 22.6	1.3660
DMC with saturated sodium methyl carbonate	1.3673, 22.6	1.3659
DMC with saturated dimethyl oxalate	1.3866, 22.7	1.3853
0.5 M $NaPF_6$ in DMC	1.3671, 23.2	1.3659
1 M $NaPF_6$ in DMC	1.3668, 23.2	1.3656
2 M $NaPF_6$ in DMC	1.3649, 23.1	1.3636
Artificial "degraded" electrolyte, Route I	1.3759, 23.7	1.3750
Artificial "degraded" electrolyte, Route II	1.3655, 24.6	1.3652

*The sample temperature measured by the refractometer; #The first four used the thermal coefficient of DMC, while the other used the one of $NaPF_6$/DMC

Note S1. Artificial "degraded" electrolytes

We prepared artificial "degraded" electrolytes according to the decomposition routes of DMC in Fig. 4g. Here shows the calculated evolution of composition during the "decomposition". Imagine we prepare 4 mL pristine electrolyte, 1 M $NaPF_6$ in DMC, there is 4 mL DMC (*i.e.*, 4.28 g, 48 mmol) and 1 M $NaPF_6$ (*i.e.*, 4 mmol, 671.8 mg). To estimate the quantity of irreversible reactions occurring in Fig. 4 (GITT test), we assumed all the electrochemistry to be irreversible. Namely, we have 599 mAh (*i.e.*, 22 mmol) electrons for irreversible reactions of 5.3 mL electrolyte (for one 18650 cell), namely, 452 mAh (*i.e.*, 17 mmol) for 4 mL electrolyte.

According to Route I of DMC degradation (Fig. 4g), 17 mmol electrons will convert 17 mmol DMC into 17 mmol sodium methoxide and roughly 8.5 mmol dimethyl oxalate. Thus, the composition of "degraded" electrolyte of Route I will be 17 mmol (*i.e.*, 918 mg) sodium methoxide, 8.5 mmol (*i.e.*, 1004 mg) methyl oxalate, 31 mmol (*i.e.*, 2792 mg) DMC, and 4 mmol (671.8 mg) $NaPF_6$.

According to Route II of DMC degradation (Fig. 4g), there was an unknown ratio of converting sodium methyl carbonate into sodium carbonate. As an estimation, we assumed 50% of the sodium methyl carbonate would be converted. Thus, 34/3 mmol and 17/3 mmol electrons will be used for DMC → sodium methyl carbonate and sodium methyl carbonate → sodium carbonate, respectively. Consequently, 34/3 mmol DMC will be consumed with the generation of 34/3 mmol sodium methyl carbonate, 17/3 mmol of which will be consumed and converted into sodium carbonate. Overall, the composition of "degraded" electrolyte of Route II will be 17/3 mmol (*i.e.*, 555 mg) sodium methyl carbonate, 17/3 mmol (*i.e.*, 601 mg) sodium carbonate, 37 mmol (*i.e.*, 3303 mg) DMC, and 4 mmol (671.8 mg) $NaPF_6$.

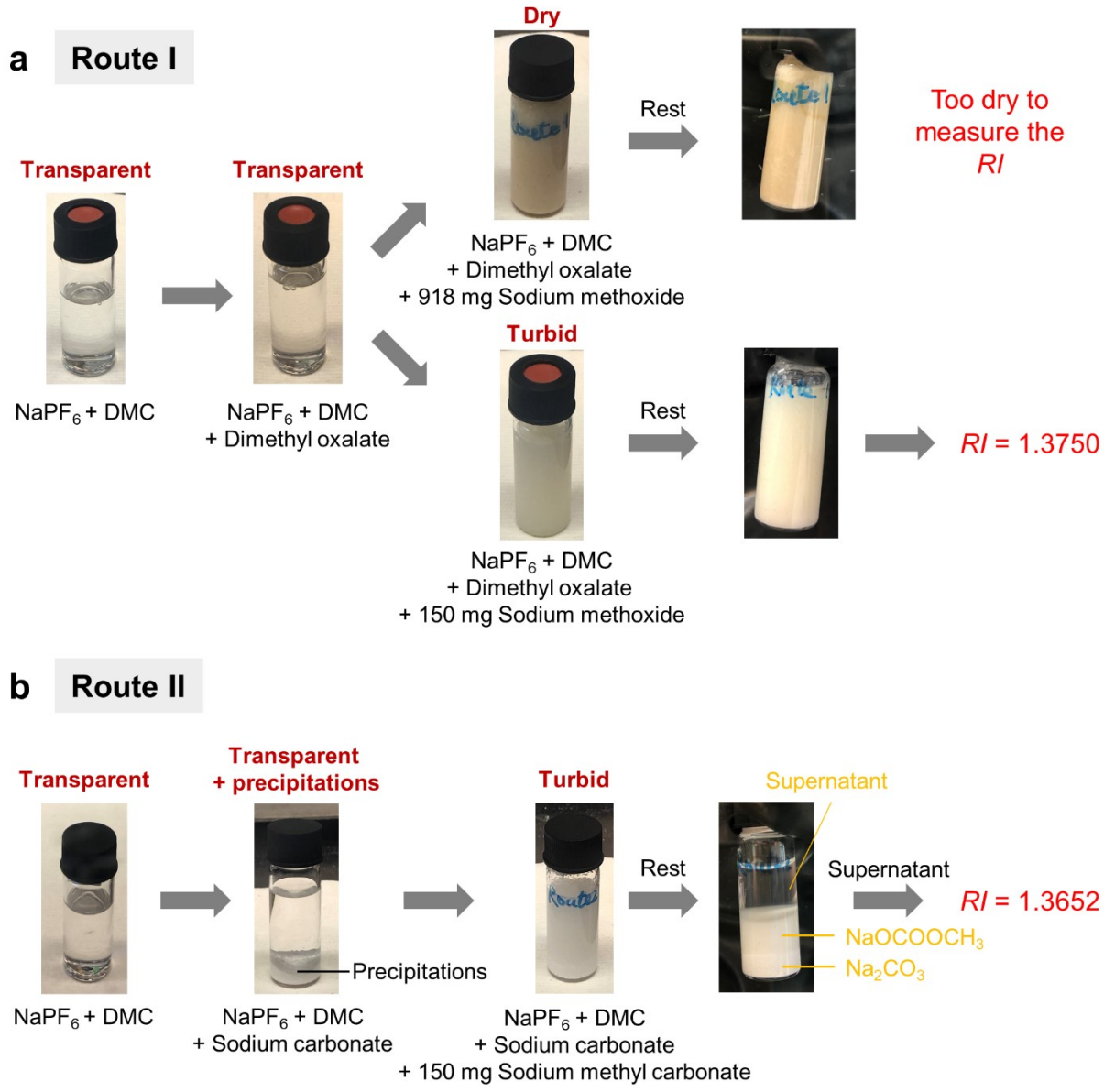

Fig. S10 Turbidity and *RI* of artificial "degraded" electrolytes. (a and b) The optical photos of as-prepared artificial "degraded" electrolyte solutions according to Route I (a) and Route II (b) as described in Fig. 4g and Note S1. At the beginning, we put all the chemicals together for Route I and found that it was too dry to take the liquid for the commercial refractometer. Thus, we prepared the solutions stepwise and mixed those that were highly soluble first. In (a), we observed that the "$NaPF_6$ + DMC" and "$NaPF_6$ + DMC + dimethyl oxalate" were transparent without depositions; however, when we added 150 mg sodium methoxide, the solution became very turbid. Even though we kept the solution still overnight, the solution remained turbid and became kind of gel. We took the solution for the commercial refractometer, and the *RI* was measured to be 1.3759 RIU at 23.7 °C (~1.3750 RIU at 25 °C), which was higher than the one of $NaPF_6$/DMC (~1.3656 RIU at 25 °C). We did not try to add more sodium methoxide because (1) The sodium methoxide was already saturated, and the further addition would increase the turbidity but may not change the *RI* of the solution; (2) The more sodium methoxide prevented us from taking the solution for *RI* measurements. In (b), though $NaPF_6$/DMC was transparent, the precipitation appeared once sodium

carbonate was added. Interestingly, the stratification was immediately seen. Once the sodium methyl carbonate was added (150 mg rather than 555 mg for the same reasons for sodium methoxide), the solution became turbid. However, after one night, we saw the stratification with supernatant, sodium methyl carbonate, and sodium carbonate from top to bottom. We then took the supernatant, whose *RI* was measured to be 1.3655 RIU at 24.6 °C (~1.3652 RIU at 25 °C), which was quite close to the one of $NaPF_6$/DMC (~1.3656 RIU at 25 °C). Overall, the value of Route I (~1.3750 RIU at 25 °C) is closer to the final *RI* (1.3739 RIU at 25 °C) measured by TFBG in Fig. 4f than the one of Route II (~1.3652 RIU at 25 °C). The difference between 1.3739 and 1.3750 indicates the possible occurrence of Route II and the decomposition of $NaPF_6$. This is consistent with the fact seen in Fig. 4f that the *RI* did not always increase upon different titrations.

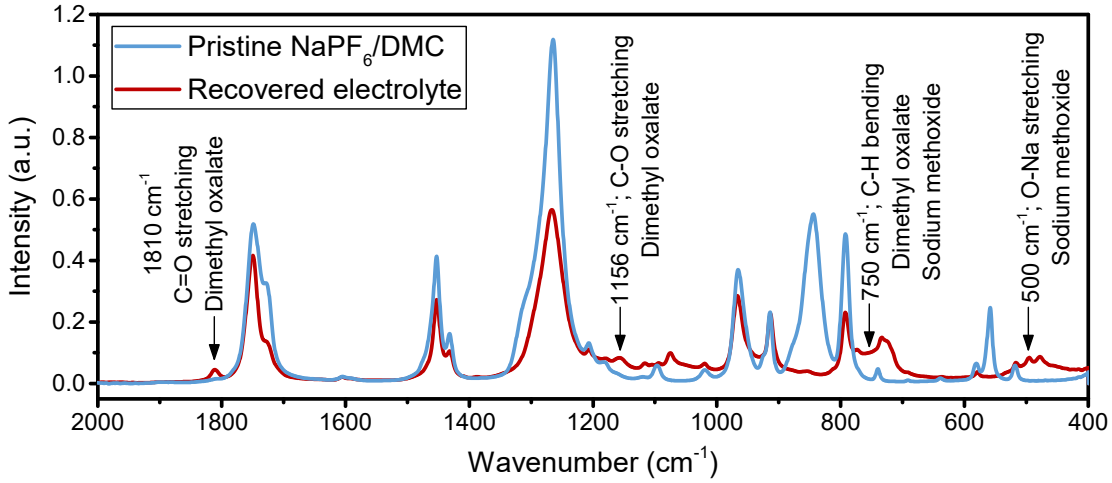

Fig. S11 The FT-IR spectra of the degraded $NaPF_6$/DMC electrolyte recovered from the cells. The FT-IR was conducted in an Ar-filled glove box with the electrolyte recovered from Swagelok cells.

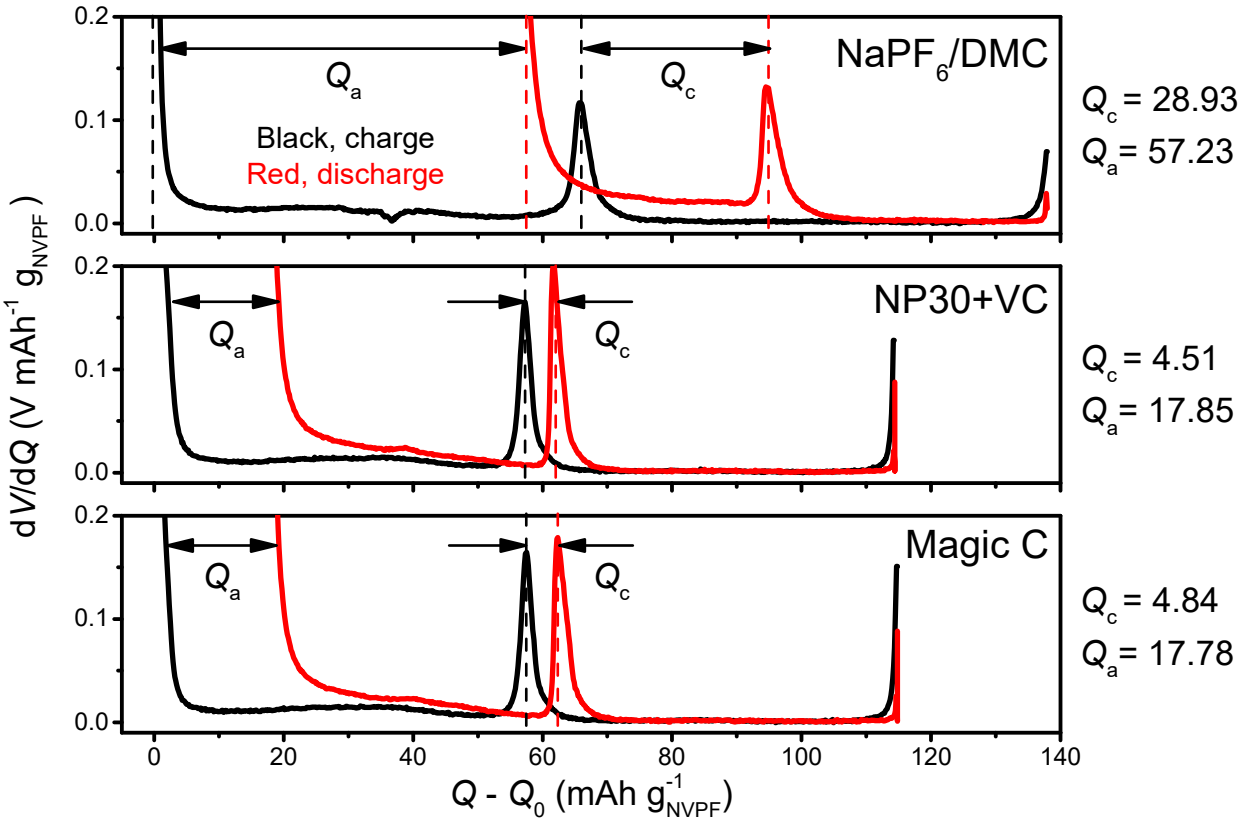

Fig. S12 The d*V*/d*Q* analysis of the first cycle during SEI formation. The d*V*/d*Q* analysis of the first charge (black) and discharge (red) profiles during the SEI formation of NVPF/HC 18650 cells containing $NaPF_6$/DMC, NP30+VC, and Magic C electrolytes in a 25 °C oven are shown in the top, middle, and bottom panels, respectively. The black peak shifts to left from $NaPF_6$/DMC to NP30+VC and Magic C, indicating the decreased oxidation of the species that were formed on HC[S8]. Besides, as demonstrated in our previous paper[S9], the two variables, Q_a and Q_c, quantify the parasitic reactions occurring in the HC and NVPF, respectively. We found that Q_a are larger than Q_c in these three electrolytes, confirming that the prevalence of parasitic reactions in HC over NVPF. Besides, the reductions of Q_a and Q_c from $NaPF_6$/DMC to NP30+VC and Magic C are consistent with the temperature and refractive index results shown in Fig. 5a.

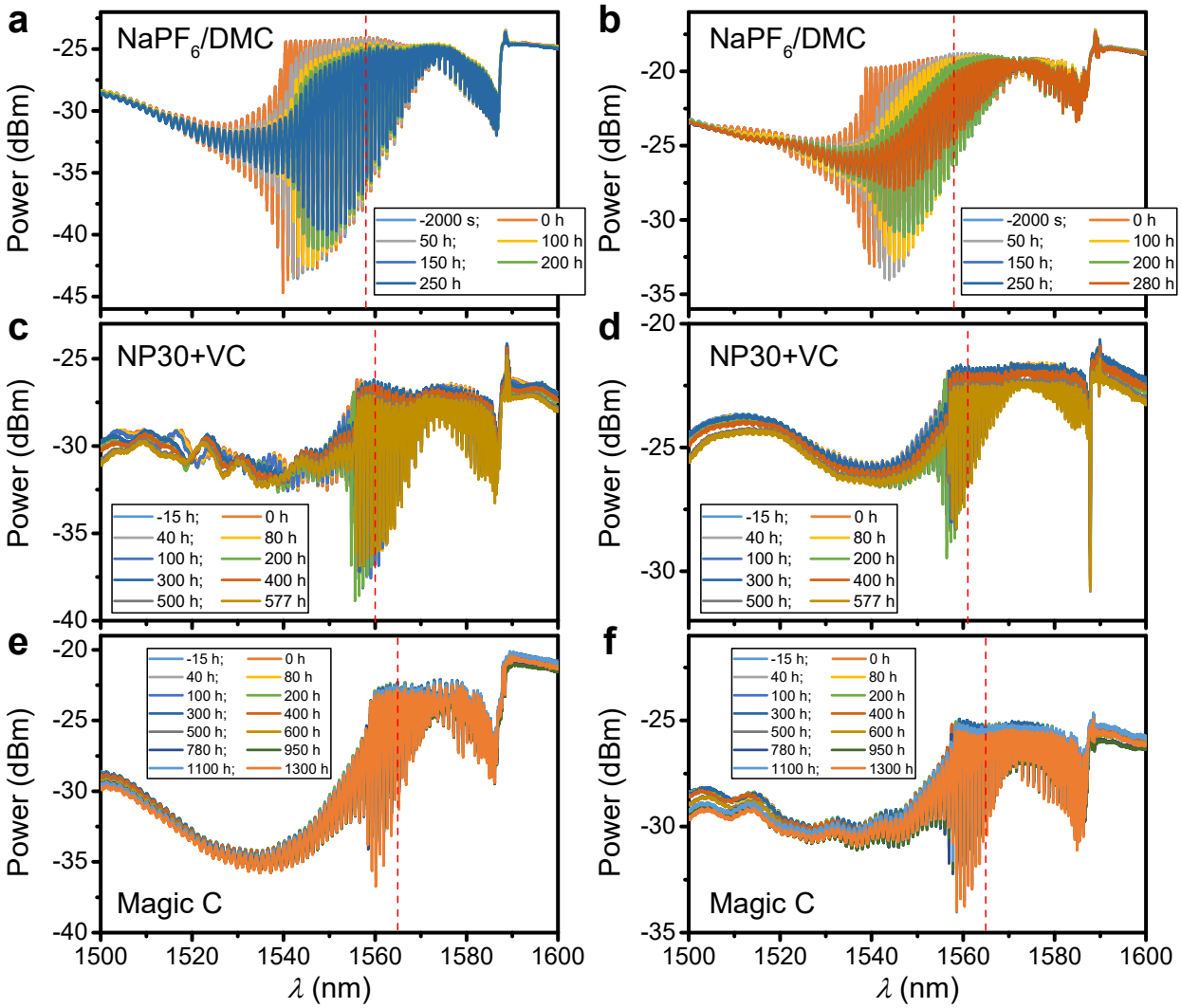

Fig. S13 The TFBG spectra upon the electrochemical tests. (a-f) The TFBG spectra corresponding to electrolytes of $NaPF_6$/DMC (a and b), NP30+VC (c and d), and Magic C (e and f). Note that two cells were tested for each batch, providing two graphs for each here. The red vertical dash line in each graph indicates the position of resonance to calculate the *A,* as discussed in Fig. 4d,e. We noticed the differences between the pristine spectra (power, prominent ghost mode in d, etc.) of TFBGs originating from the TFBG inscription process; consequently, we calibrated each sensor individually. We expect that the TFBGs with identical spectra and highly repeatable responses can be achieved by further optimizing the inscription process. Besides, some slight decreases of background power are observed after long-term tests (c-f), which may be ascribed to the minor damage of the gold reflector. This issue needs to be addressed by either the transmission measurement or the optimization of the coating parameters (such as thicker coating or enhancing the interfacial bonding).

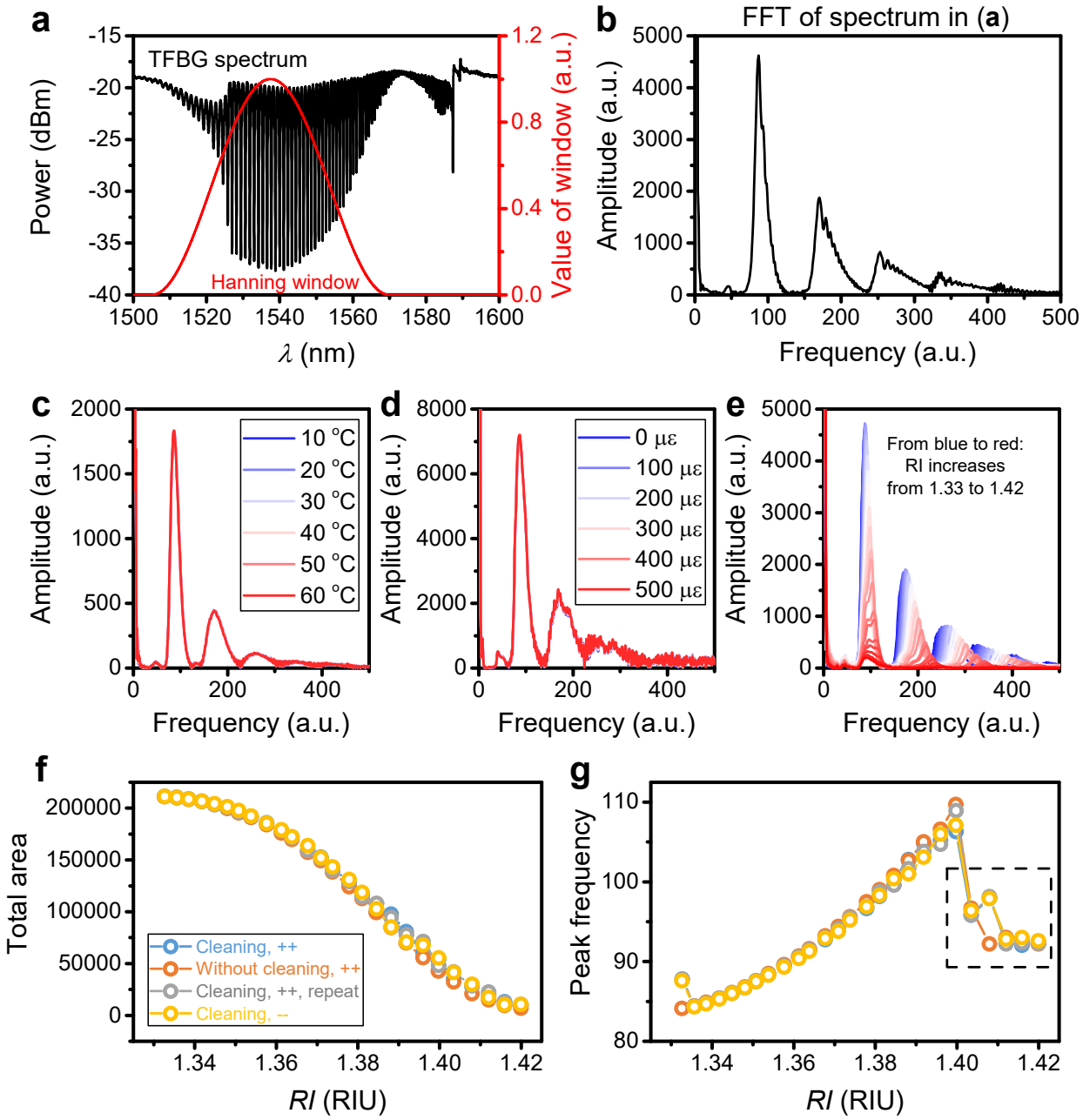

Fig. S14 Fast Fourier Transform (FFT) of the TFBG spectra. (a) An example of TFBG spectrum (left axis, black, 10 wt.% sucrose) and the Hanning window (right axis, red). The Hanning window was applied to reduce the noise in the FFT result. (b) The FFT of the TFBG spectrum in (a). The FFT spectrum was computed by taking the absolute value of the FFT of the product of the TFBG spectrum and the Hanning window, namely, abs(FFT(H.*Spectrum)). Interestingly, the number of peaks in FFT is significantly reduced in comparison to the one in the TFBG spectrum. (c-e) The FFT spectra in response to temperature (c), strain (d), and refractive index (e). In (e), the *RI* gradually varies from 1.33 (blue) to 1.42 (red). Surprisingly, no distinguishable changes are spotted upon the temperature and strain variations, while the FFT spectra significantly evolve with the refractive index. These results suggest the possibility of adopting the FFT spectrum for the exclusive calculation of *RI* measured by TFBG. (f and g) The total area of the FFT spectra

with the frequency ranging from 50 to 550 (f) and the frequency of the peak at a frequency of ~100 (g) in four *RI* calibrations of the same TFBG as depicted in Fig. S5. The dashed rectangle in (g) implies the unreliability of the data due to the profound changes in the peak shape and amplitude as seen in (e). We also explored other features, including the amplitude, the area, the centroid, and the full width at half maximum (FWHM) of a single peak, which were less representative than the above two and thus not shown here. Remarkably, the four responses in (f and g) are largely overlapped with each other, indicating a solution to the wavelength drift of TFBG as discussed in Fig. S5. However, some minor differences remain in (f and g), for example, in the *RI* range of 1.38 and 1.41, which deserves further investigations by experiments and data treatments.

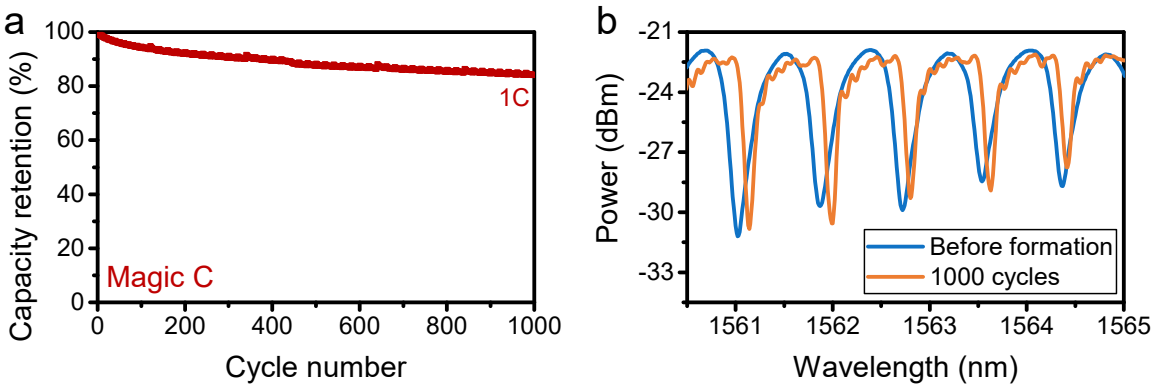

Fig. S15 The TFBG's bandwidth evolution upon long cycling. (a) The capacity retention of the NVPF/HC 18650 cell as a function of cycle number in the 25 °C oven with the electrolyte of Magic C. (b) The enlarged TFBG spectra to examine the bandwidth variations, because the corrosion of HF on TFBG manifests itself by the enlarged bandwidth as a consequence of the mode escaping[S10]. Clearly, there is no enlarged bandwidth after 1000 cycles, that is, the HF corrosion effect is not visible. Note that the slight change in background may possibly come from the breakdown and repairment of the interrogator in the middle of the long cycling.

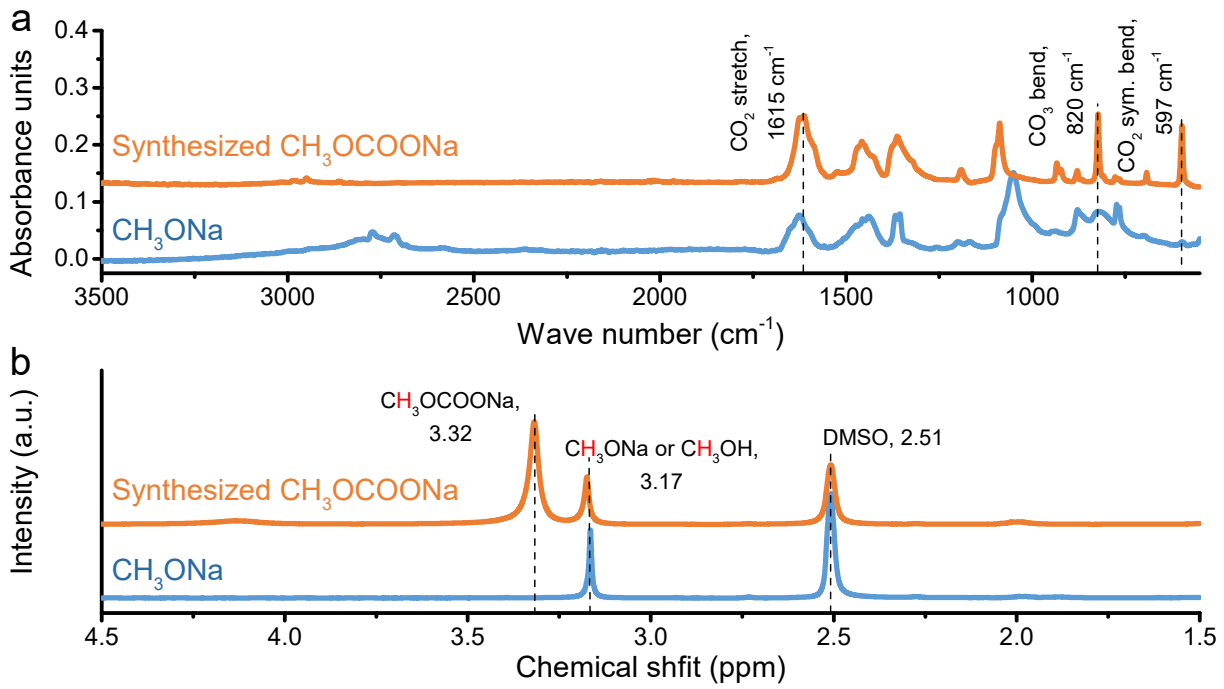

Fig. S16 FT-IR and NMR spectra of sodium methoxide and as-synthesized sodium methyl carbonate. (a) The FT-IR spectra of CH_3ONa and the as-synthesized $CH_3OCOONa$. The appearances of CO_2 stretching, CO_3 bending, and CO_2 symmetric bending at 1615, 820, and 597 cm^{-1}, respectively, imply the successful introduction of CO_2 into the sodium methoxide. The assignments of the peaks referred to the literature[S8, 11]. (b) The NMR spectra of CH_3ONa and the as-synthesized $CH_3OCOONa$. The samples were dispersed into the deuterated dimethyl sulfoxide (DMSO-d6) as an internal reference. The new peak at the chemical shift of 3.32 ppm supports the formation of $CH_3OCOONa$, though the peak at 3.17 ppm may imply the traces of unreacted CH_3ONa or CH_3OH (the solvent for the reaction[S8]). The assignments of the peaks referred to the literature[S8, 12]. The FT-IR and NMR results consistently confirm the successful synthesis of $CH_3OCOONa$.

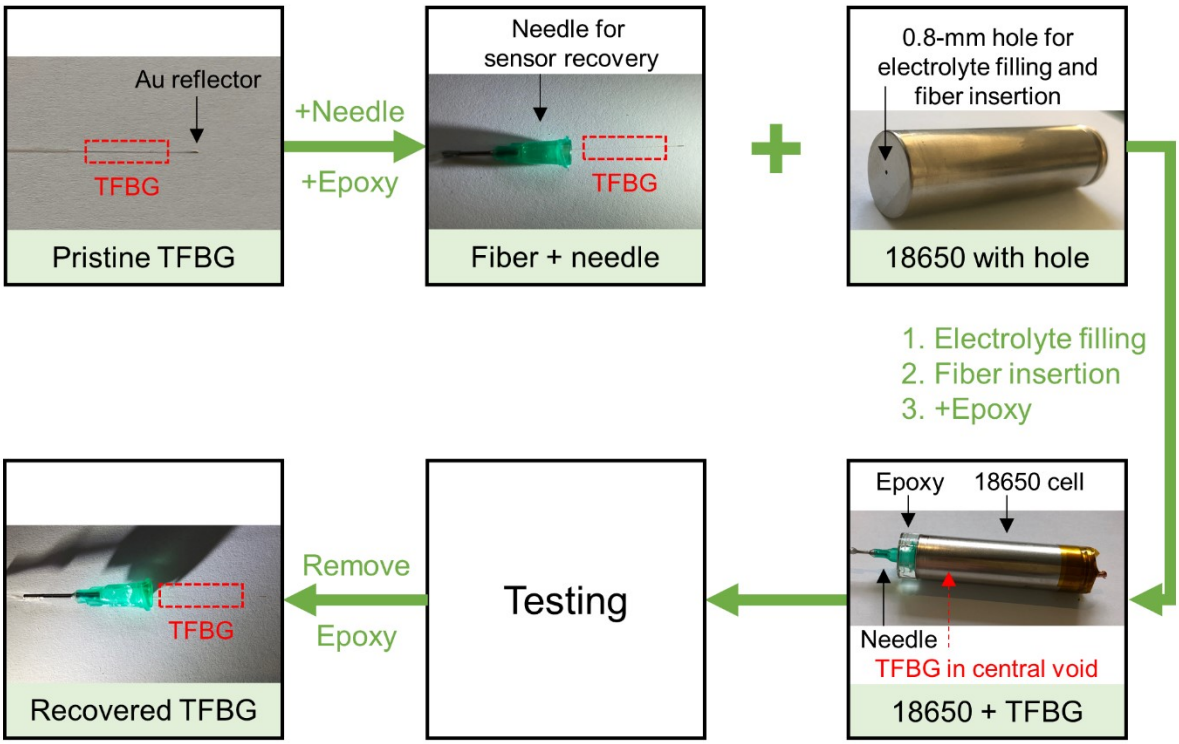

Fig. S17 The detailed procedure for TFBG insertion. As discussed in Methods - Integration of TFBG into the 18650 cells, the TFBG was pre-bonded with a needle by epoxy for future reuse. The TFBG was inserted into the central void of jelly roll via the 0.8-mm hole with the grating region close to the negative pole. They were then sealed by epoxy, which took 24 hours for curing.

Supplementary references

S1. C.-F. Chan, C. Chen, A. Jafari, A. Laronche, D. J. Thomson and J. Albert, *Appl. Opt.*, 2007, **46**, 1142-1149.
S2. C. Chen and J. Albert, *Electron. Lett.*, 2006, **42**, 1027-1028.
S3. J. Huang, L. A. Blanquer, J. Bonefacino, E. R. Logan, D. A. Dalla Corte, C. Delacourt, B. M. Gallant, S. T. Boles, J. Dahn, H.-Y. Tam and J. M. Tarascon, *Nat. Energy*, 2020, **5**, 674-683.
S4. R. Waxler and C. Weir, *Journal of research of the National Bureau of Standards. Section A, Physics and chemistry*, 1963, **67**, 163.
S5. L. Htein, Z. Liu, D. Gunawardena and H.-Y. Tam, *Optics express*, 2019, **27**, 9655-9664.
S6. M. C. P. Huy, G. Laffont, V. Dewynter, P. Ferdinand, L. Labonté, D. Pagnoux, P. Roy, W. Blanc and B. Dussardier, *Optics Express*, 2006, **14**, 10359-10370.
S7. F. Liu, X. Zhang, T. Guo and J. Albert, *APL Photonics*, 2020, **5**, 076101.
S8. G. Yan, D. Alves-Dalla-Corte, W. Yin, N. Madern, G. Gachot and J.-M. Tarascon, *J. Electrochem. Soc.*, 2018, **165**, A1222-A1230.
S9. G. Yan, R. Dugas and J.-M. Tarascon, *J. Electrochem. Soc.*, 2018, **165**, A220.
S10. M. Sypabekova, S. Korganbayev, Á. González-Vila, C. Caucheteur, M. Shaimerdenova, T. Ayupova, A. Bekmurzayeva, L. Vangelista and D. Tosi, *Biosensors and Bioelectronics*, 2019, **146**, 111765.
S11. D. Aurbach, M. Daroux, P. Faguy and E. Yeager, *J. Electrochem. Soc.*, 1987, **134**, 1611.
S12. K. Xu, G. V. Zhuang, J. L. Allen, U. Lee, S. S. Zhang, P. N. Ross Jr and T. R. Jow, *J. Phys. Chem. B*, 2006, **110**, 7708-7719.